



## Scale attachment and detachment: The role of hydrodynamics and surface morphology

Løge, Isaac A.; Bentzon, Jakob R.; Klingaa, Christopher G.; Walther, Jens H.; Anabaraonye, Benaiah U.; Fosbøl, Philip L.

*Published in:*  
Chemical Engineering Journal

*Link to article, DOI:*  
[10.1016/j.cej.2021.132583](https://doi.org/10.1016/j.cej.2021.132583)

*Publication date:*  
2022

*Document Version*  
Publisher's PDF, also known as Version of record

[Link back to DTU Orbit](#)

*Citation (APA):*  
Løge, I. A., Bentzon, J. R., Klingaa, C. G., Walther, J. H., Anabaraonye, B. U., & Fosbøl, P. L. (2022). Scale attachment and detachment: The role of hydrodynamics and surface morphology. *Chemical Engineering Journal*, 430, Article 132583. <https://doi.org/10.1016/j.cej.2021.132583>

---

### General rights

Copyright and moral rights for the publications made accessible in the public portal are retained by the authors and/or other copyright owners and it is a condition of accessing publications that users recognise and abide by the legal requirements associated with these rights.

- Users may download and print one copy of any publication from the public portal for the purpose of private study or research.
- You may not further distribute the material or use it for any profit-making activity or commercial gain
- You may freely distribute the URL identifying the publication in the public portal

If you believe that this document breaches copyright please contact us providing details, and we will remove access to the work immediately and investigate your claim.



# Scale attachment and detachment: The role of hydrodynamics and surface morphology

Isaac A. Løge<sup>a,\*</sup>, Jakob R. Bentzon<sup>b</sup>, Christopher G. Klingaa<sup>b</sup>, Jens H. Walther<sup>b,c</sup>, Benaiah U. Anabaraonye<sup>d</sup>, Philip L. Fosbøl<sup>a</sup>

<sup>a</sup> Department of Chemical Engineering, Technical University of Denmark, Kgs. Lyngby, 2800, Denmark

<sup>b</sup> Department of Mechanical Engineering, Technical University of Denmark, Kgs. Lyngby, 2800, Denmark

<sup>c</sup> Computational Science and Engineering Laboratory, ETH, Zürich CH-8092, Switzerland

<sup>d</sup> Danish Hydrocarbon Research and Technology Centre, Technical University of Denmark, Kgs. Lyngby, 2800, Denmark

## ARTICLE INFO

### Keywords:

Fouling mechanisms  
Surface roughness  
CFD  
Crystallization fouling  
Hydrodynamics

## ABSTRACT

Crystallization fouling presents a significant challenge in a wide range of industries. Accurate understanding of crystal formation is crucial for planning preventative measures and maximizing the effectiveness of maintenance interventions. In this study, we demonstrate that understanding net deposition rates depends on the knowledge of the detachment mechanisms and deposition distribution characteristics. We quantify deposition in a once-through flow set-up and visualize crystal formation through high-resolution X-ray micro-computed tomography scanning. Additionally, we quantify the height distribution of deposited crystals through computed surface texture parameters. Finally, we use computational fluid dynamics, implementing large-eddy simulations turbulence modelling and Eulerian transport of chemical species, to describe bulk and wall reactions and quantify energy and mass transport in turbulent eddies. Results show that attachment and detachment processes depend on fluid hydrodynamics; the influx of material determines the overall deposition to the surface, while the deposition pattern is governed by the surface morphology of the initial surface morphology. Our findings provide a foundation for understanding fouling mechanisms and present a template for developing more accurate prediction models.

## 1. Introduction

Crystallization fouling, i.e., scaling, occurs due to the precipitation and subsequent adhesion of crystals on surfaces. The presence of scaling has a wide range of deleterious effects in several industries. Examples include increased production costs in water treatment processes [1–4], flow assurance challenges in the petroleum industry [5,6], sub-optimal performance of heat exchangers [7,8], and reduced energy transfers in for geothermal energy systems [9].

Effective scale prevention and removal strategies depend on an accurate understanding of the processes preceding surface adhesion [10, 11]. Scale formation is a multi-step complex process involving nucleation, adhesion, and growth [12,13]. Chemical inhibitors that either slow nucleation kinetics or prevent crystal growth are widely used [14]. However, these can be detrimental to aquatic life [15]. Deposited crystals are either removed mechanically or through chemical means [16]. The ability to predict the magnitude and location of crystal formation is vital for the planning and managing of both chemical inhibition and

removal interventions [17]. Therefore, accurate prediction models are critical.

Nucleation and crystal growth combined with hydrodynamics are complex processes to simulate accurately [18,19]. When modelling the rate of scale formation, two key approaches have been presented in the literature. In the first approach, kinetic rate laws for scale formation are proposed based solely on correlations between various process parameters and the measured deposition rate [20–23]. This approach primarily relies on fitting experimental data and does not account for the actual mechanisms at play. Due to the ease of implementation, this approach is widely used. The second approach explicitly accounts for the competition between adhesion and detachment rates on the net surface deposition rate [24,25]. Recently, a mathematical framework based on the second approach was presented [26,27]. Here an increase in flow was found to result in lower net deposition rates [27]. This is in agreement with the observation that detachment processes are considered correlated with the shear stress exerted by the fluid on

\* Corresponding author.

E-mail address: [isacl@kt.dtu.dk](mailto:isacl@kt.dtu.dk) (I.A. Løge).

the surface [25]. However, due to the limited understanding of detachment mechanisms, accurate prediction of net scale deposition is challenging [28,29]. This is reflected in conflicting findings: Higher net deposition rates have been observed both in systems with increased [20,30,31] and decreased [26,27,32–34] fluid velocities and shear stresses. An increase in surface roughness has been reported to increase the scale formation rate [35,36], whereas other studies found weak or no correlation [30]. Surface texture has been reported to affect the morphology of the formed crystals [37,38]. Anti-scaling materials have been synthesized by engineering low energy surfaces [39].

In this study, we investigate the complex interplay between fluid flow and surface morphology on scale deposition. Two key experimental variables were studied: The fluid hydrodynamics – laminar and turbulent flow regimes – and surface morphology of the deposition cells – smooth and rough. The laminar flow domain represented a low material influx regime where the transport of material to the surface is diffusion-limited. In the turbulent flow regime, where there is a high material influx, the transport limitation was reduced and the effect of a fluid–wall coupling in a turbulent flow domain was illustrated. In addition, we investigated the interaction areas of engineered surfaces resembling that of production equipment at both the beginning (i.e., smooth) and at the end [40] (i.e., rough) of a life cycle. In this study, we engineered threaded surfaces to investigate the role of surface roughness. The key feature of the fluid–wall interaction is the effect of the transport as the boundary layers are affected by the modulation of the bulk turbulence by the surface profile.

We conducted experiments using a once-through flow set-up with a constant flow of BaSO<sub>4</sub> saturated brine through the reactor cell. The magnitude of crystal growth is quantified through gravimetric analysis. We use high-resolution X-ray micro-computed tomography (CT) scanning to visualize scale deposition. The surface texture parameters of the scaled deposition cells are quantified using a custom-written Python code [41].

We perform numerical simulations based on computational fluid dynamics (CFD) applying large eddy simulation (LES) turbulence modelling, and Eulerian transport of the chemical species. The CFD simulations are used to illustrate the effects of hydrodynamics on the transport of reacting species.

These cases are designed to explore and understand how detachment processes are flow-dependent. Based on these case studies, we demonstrate the importance of reintroducing an accurate description of the detachment processes to understand overall scale build-up.

## 2. Materials and method

### 2.1. Materials

Two brines were prepared: a 2.04  $\frac{\text{mmol}}{\text{kg H}_2\text{O}}$  Na<sub>2</sub>SO<sub>4</sub> and a BaCl<sub>2</sub> solution with a concentration of 0.972  $\frac{\text{mmol}}{\text{kg H}_2\text{O}}$ . Both solutions were prepared with de-ionized water (resistivity 18.2 MΩ cm) at ambient conditions.

### 2.2. The flow set-up

A custom flow set-up has been built (see Fig. 1), which allows for the investigation of crystal growth and deposition under single throughput flow conditions. Fluids were transported using Masterflex® peristaltic pumps, with an L/S High-Performance Pump Head. Temperature control was achieved with a thermostatic bath. All experiments were performed at a temperature of 60 °C. Mixing of brines was done in a T-piece with an outlet of a 1/8 inch diameter plastic tube which was 14.5 cm long. A custom-built deposition cell was introduced after the plastic line (see Fig. 1a) with the portion in contact with the mixed brine solution being made of steel and the other compartment made of aluminium. The cell outlet was connected to a 55.5 cm long, 1/8 inch diameter plastic tube going to a waste tank.

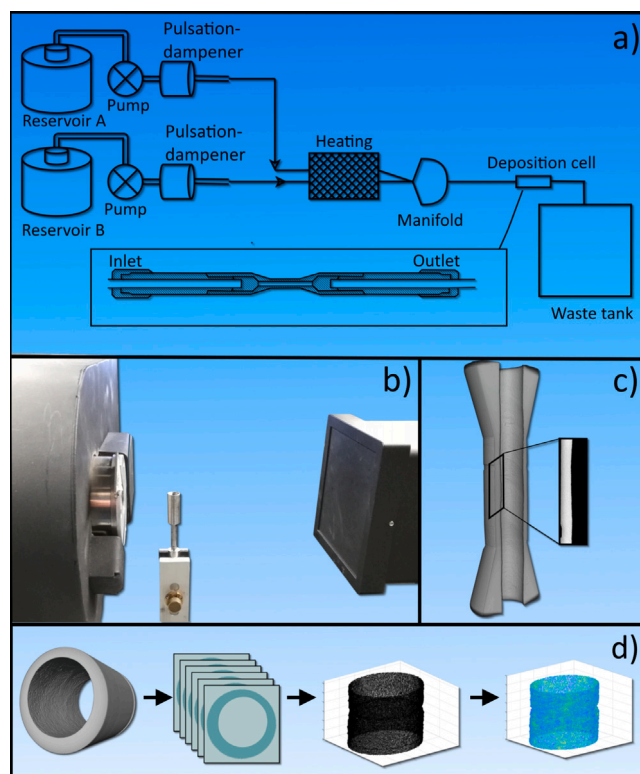


Fig. 1. Description of the workflow utilized in this work. Detailed descriptions of (a), (b) and (d) are found in Section 2.4, 2.5, and 2.7.

### 2.3. Fabrication of the deposition cell

The cells were sampled and lathed from a tube of X-52 steel. The surface finish of the cell was fabricated in two ways: One smooth and one threaded. The threaded surface was made using an ISO M3 × 0.5 thread cutting tap. The inner diameters of both cells were 3 mm. The nominal surface areas of the smooth and threaded cells were 2.83 cm<sup>2</sup> and 6.13 cm<sup>2</sup>, respectively. The surface area,  $A$ , of the threaded cell was calculated as

$$A = 1.625\pi LD \quad (1)$$

where  $L$  is the length of the cell (3 cm), and  $D$  is the diameter of the cell in the threading valleys (0.4 cm).

### 2.4. The experimental procedure

We investigated the effect of the interplay between flow rate and surface morphology on scale deposition. The experimental conditions investigated can be found in Table 1. Before each experiment, upstream flow lines of the deposition cell were flushed with de-ionized water for a minimum of five minutes to ensure proper cleaning and no leaks. Each cell was weighed before and after deposition. After the mixing point, the cell and plastic lines were positioned in an upright manner, allowing the flow to stabilize and ensuring that no additional turbulence was introduced due to kinks in the tubing. The injected flow rates were 60 mL/min and 280 mL/min for the laminar and turbulent flow, respectively. Brines were injected at a 1:1 volumetric ratio. At the end of each experiment, the cell was rinsed with de-ionized water and placed in an oven to dry at 120 °C for four hours. To test the reproducibility of the experimental procedure, one of the turbulent experiments was repeated four times. This resulted in a relative standard deviation of 2.9% (see Supplementary Material).

**Table 1**

Experimental conditions investigated:  $t$  = experimental duration,  $Pa$  = arithmetic mean height,  $VtHd$  = Valley to height distance,  $A$  = surface area.

Name	Re [-]	$t$ [min]	$Pa$ [ $\mu\text{m}$ ]	$VtHd$ [mm]	$A$ [ $\text{cm}^2$ ]
[Laminar, smooth]	1080	30	6.44	0.0	2.83
[Laminar, smooth]	1080	90	7.26	0.0	2.83
[Laminar, smooth]	1080	180	5.26	0.0	2.83
[Laminar, threaded]	1080	30	5.86	0.5	6.13
[Laminar, threaded]	1080	90	5.83	0.5	6.13
[Laminar, threaded]	1080	180	7.09	0.5	6.13
[Turbulent, smooth]	4808	15	8.93	0.0	2.83
[Turbulent, smooth]	4808	30	7.46	0.0	2.83
[Turbulent, smooth]	4808	60	8.71	0.0	2.83
[Turbulent, threaded]	4808	15	8.02	0.5	6.13
[Turbulent, threaded]	4808	30	5.79	0.5	6.13
[Turbulent, threaded]	4808	60	8.74	0.5	6.13

## 2.5. CT scanning

CT scanning of the cells after the experiment was performed with a ZEISS XRadia 410 Versa. 995 projections were acquired per sample over  $360^\circ$  with a beam intensity of 120 kV, where each projection had an exposure time of 3–15 s and an objective of  $4\times$  was used. The total volume of the tomographies was  $2.56 \text{ mm}^3$  and a voxel size of  $4 \mu\text{m}$ . Furthermore, all cells were scanned with a field of view of  $1069 \text{ mm}^3$ , which was large enough to capture the whole cell in which deposition occurred. This was done to verify that the smaller segments of the cells, which were used for most of the analyses presented in this study, were representative of the whole cell.

## 2.6. Computational Fluid Dynamics

CFD modelling is carried out using the finite volume method implemented in STAR-CCM+ version 15.06. A CFD model is implemented with simplified reaction kinetics to provide insights into the effect of the hydrodynamics on the transport of the reactants. The CFD model is based on work performed in a recently published study [19]. The brine is assumed incompressible, and the influence of the solutes on the solvent density and viscosity was neglected. The temperature field is fixed isothermally to  $60^\circ\text{C}$ . The fluid density is set to  $983.2 \text{ kg/m}^3$  and the dynamic viscosity to  $0.466 \times 10^{-3} \text{ kg/(m s)}$ .

As all length and time scales are not resolved by the computational grid, spatial filtering using LES turbulence modelling was applied. This yields a generalized conservation equation of a conserved quantity  $\phi$ :

$$\frac{\partial \bar{\phi}}{\partial t} + \frac{\partial u_i \bar{\phi}}{\partial x_i} - \frac{\partial}{\partial x_i} D \frac{\partial \bar{\phi}}{\partial x_i} = \bar{S} \quad (2)$$

where the indexing  $i$  follows tensor notation, the overbar denotes a spatially averaged quantity,  $D$  is the diffusivity of  $\phi$  and  $S$  covers source terms. The model conserves mass ( $\phi = \rho$ ), momentum ( $\phi = \rho u_i$ ), and solute concentration ( $\phi = m_s$ ) where  $u_i$  is the velocity vector,  $\rho$  the liquid density and  $m_s$  the molality of a given solute.

The Pitzer activity model [42] is implemented using an in-house developed C library to compute the saturation ratio (SR) of barium sulfate:

$$\text{SR} = \frac{\alpha_{\text{Ba}^{2+}} \alpha_{\text{SO}_4^{2-}}}{K_{\text{BaSO}_4}} \quad (3)$$

Here  $\alpha_{\text{Ba}^{2+}}$  and  $\alpha_{\text{SO}_4^{2-}}$  are the activities of barium and sulphate.  $K_{\text{BaSO}_4}$  is the equilibrium constant.

A reaction model is implemented in both the bulk and on the wall. The bulk reaction term is modelled as a second-order reaction:

$$r_{\text{Ba}^{2+}} = r_{\text{SO}_4^{2-}} = (\text{SR} - 1)k\alpha_{\text{Ba}^{2+}}\alpha_{\text{SO}_4^{2-}} \quad (4)$$

Similar to the previously mentioned paper, [19],  $k$  is obtained from a second order polynomial fitting of batch experimental data combined with data from Zhen-Wu et al. [43]. Bulk precipitates are transported

passively with the flow. No attachment mechanism is implemented. The surface reaction rate is implemented with a similar second order reaction, using a surface rate constant  $k_s$  set to  $1 \text{ m/s}$  to calculate a boundary flux  $j$ :

$$j_{\text{Ba}^{2+}} = j_{\text{SO}_4^{2-}} = (\text{SR} - 1)k_s\alpha_{\text{Ba}^{2+}}\alpha_{\text{SO}_4^{2-}} \quad (5)$$

The CFD model accounts for the deposition cell as well as the straight tubing attached on inlet and outlet. The fluid inlet is located 40 diameters of tubing upstream of the cell. The inlet conditions are modelled using a constant mass flow rate. The concentration of the inlet brine is assumed perfectly pre-mixed. The outlet is located 20 diameters of tubing downstream from the cell and is modelled using a fixed uniform atmospheric pressure. Fig. 2 illustrates the layout and dimensions of the threaded deposition cell used for the CFD model. All cell and tubing walls are modelled as no-slip walls. For the reactants the walls are modelled as sinks consuming a prescribed flux. The boundary fluxes are calculated in each boundary cell face for each time step solving Eq. (4). The actual deposition of the material is not modelled, i.e. no changes in solid geometry is implemented. The induction time for scaling under the experimental conditions investigated was calculated based on classical nucleation theory [44], and on literature parameters [45,46]. The calculated induction time was  $<1 \text{ ms}$ , consequently, nucleation processes were not accounted for in the model. Temporal discretization is performed using second order implicit time stepping with Courant numbers below one. Reported time-averaged results are sampled over 5 times the residence time of the entire domain.

The computational domain is discretized using a set of 10 prism layers near the wall in both tubing and cell to resolve boundary layer flow and diffusion. The prism layers encapsulate a polyhedral mesh core with gradual refinement going from a coarser core to finest grid near the cell wall.

In terms of surface deposition rates, modelling uncertainties from the simplification of the kinetics and thermodynamics are considerably larger compared to the uncertainties of the flow model, and thus the CFD model is aimed at describing the flow-related effects rather than as a deposition prediction model. A sensitivity study is performed to test the effect of variations to the rate constants  $k$  and  $k_w$ . While the absolute fluxes and saturation ratio fields are impacted by changing these parameters, the key conclusions remain unchanged.

As a baseline for comparison, a simple one-dimensional plug flow model (PFM) is also implemented. This model relies on an axial discretization of the cell and inlet tubing and is solved temporally through forward integration. This effectively models the kinetics without radial transport limitation and, thus, compared to the CFD model, can be used to highlight the effects of transport.

The domain of the implemented PFM comprises of the deposition cell as well as 40 cell diameters tubing upstream of the cell. The reaction model from Eq. (4) is implemented in each axial cell. All precipitated products are assumed to deposit immediately in the same cell. Thus the PFM model does not account for bulk precipitates being transported with the flow.

## 2.7. Surface analysis

The surface texture characterization performed in this study was based on the methodology proposed by Klingaa et al. [41], which uses

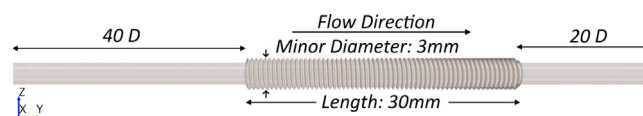


Fig. 2. Illustration of the computational domain for the threaded deposition cell.

an in-house Python code to extract surface texture information from 3D point cloud data, generated from the exported stack of images. The surface profile parameters used in this work are defined as:

$$Pa = \frac{1}{l} \int_0^l |Z(x)| dx \quad (6)$$

where  $l$  is the length of investigated surface in the flow direction,  $x$ , and  $Z(x)$  is the surface height. The spikiness,  $Pku$ , is defined as:

$$Pku = \frac{1}{Pq^4} \left( \frac{1}{l} \int_0^l Z(x)^4 dx \right) \quad (7)$$

where  $Pq$  is the variation of the surface height:

$$Pq = \sqrt{\frac{1}{l} \int_0^l Z(x)^2 dx} \quad (8)$$

If  $Pku < 3$  the profile consists of soft peaks and deep valleys. If  $Pku = 3$  the profile has an equal distribution of soft and sharp peaks and valleys. If  $Pku > 3$  the profile is characterized as being spiked [41]. These can therefore be used to quantify what kind of height distribution deposited material exhibit on a surface.  $Pa$  is the arithmetical mean height of the assessed profile, compared to the mean line of the profile, and gives a general description of the surface texture over the profile length. An increased surface roughness is likely to yield more nucleation sites.

### 3. Results and discussion

#### 3.1. Attachment and detachment of scale

The rate of scale formation in a system with a high ratio of reaction rate to transport is limited by the transport of ions to the surface. CFD was utilized to investigate the transport phenomenon of the dissolved ions. Turbulent flow is governed by an unsteady turbulent core transitioning into a thin laminar sub-layer near the wall, whereas the laminar flow remains steady and stratified through the fluid bulk. In the stratified layers, the transport of the material towards the wall is limited by diffusion, whereas within the turbulent core, small scale convection due to turbulence drastically increases the transport towards the wall [47]. Transport considerations are neglected in traditional simple reactor models such as the PFM implemented in this study.

The saturation profiles of the bulk fluid, at the investigated conditions, are shown in Fig. 3. The inserts on the right in Fig. 3 illustrate the differences in the concentration gradients near the wall. The laminar flow over the smooth surface has a steeper boundary gradient compared to that of the laminar flow over the threaded surface. This is expected as irregular surfaces are known to increase the size of the boundary layer [48]. From Fig. 3cd it can be observed that for the turbulent-threaded condition, the onset of turbulence occurs closer to the inlet than for the smooth case.

Differences in bulk flow profile affect the influx of material to the surface. To compare the influx between different conditions, Fig. 3e shows the mean material influx for all four cases. Based on these results, the laminar and turbulent flow regimes will be referred to as the low and high influx regimes, respectively.

The main difference between the CFD model and the simpler PFM reactor model is their ability to capture the effects of high vs. low ionic flux towards the cell surface. In Fig. 4 we compare the average surface flux between the CFD and PFM reactor models to put these effects into perspective. Two key aspects governs the difference between the laminar and turbulent conditions. Firstly, the turbulence significantly increases the aforementioned ionic influx, effectively shortening the diffusion time from bulk to wall. Conversely, the residence time becomes significantly lower for the turbulent flow due to the higher flow rate, and consequently, each fluid volume injected has a shorter time span to react onto the cell surface. The PFM model shows a monotonically decreasing flux in the axial direction due to consumption and thus gradually lower concentration, whereas the CFD model shows

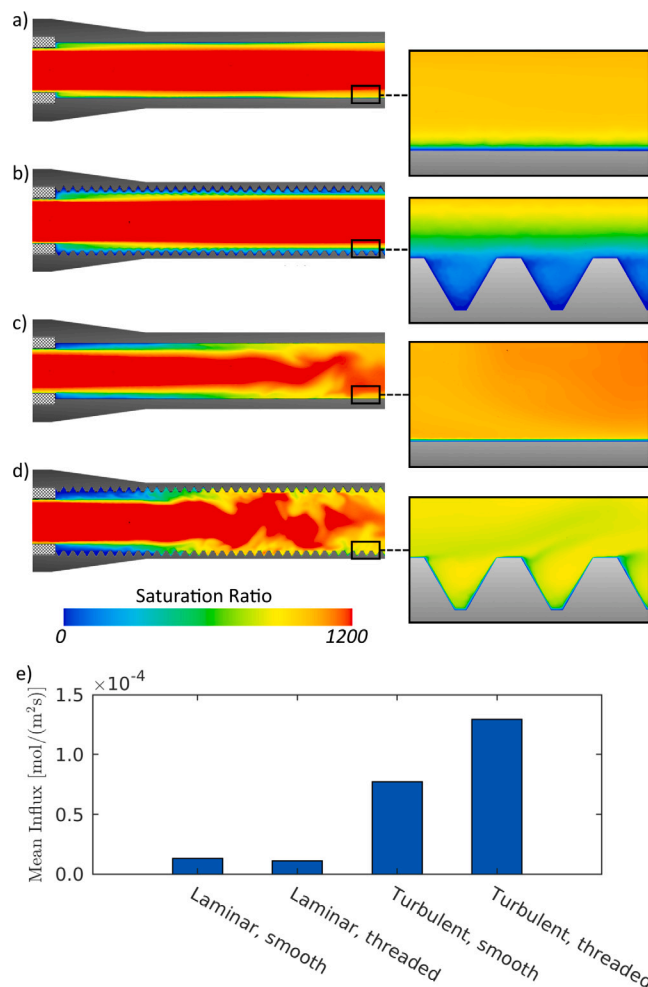


Fig. 3. Simulated bulk saturation profiles. Inserts showing the boundary layer thickness. (a) Laminar, smooth. (b) Laminar, threaded. (c) Turbulent, smooth. (d) Turbulent, threaded (e) Mean material influx.

the combination of an axially increasing flux due to dispersion and axially decreasing due to reaction. The resulting flux is reasonably uniform in the axial direction for both the smooth and threaded cells when averaging over a full pitch length for the laminar flow. In the laminar model, the magnitude of the average fluxes is also similar across the two surface conditions. While the bulk of the flow remains

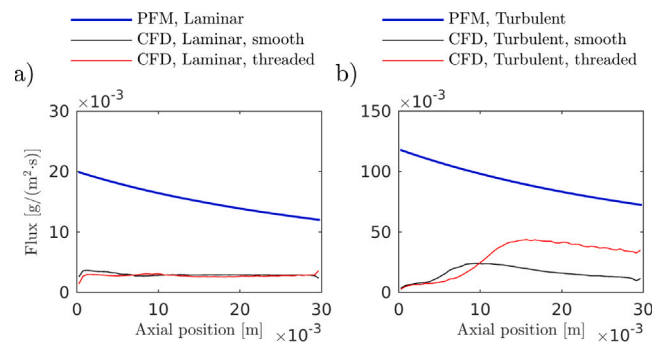


Fig. 4. Comparison between the CFD modelled distribution of deposition compared to the simple plug flow model (PFM). The plotted data from the CFD model is averaged over a thread pitch length to avoid showing the variations over the profile for the threaded models.

laminar, the threading adds rotation and thus increased mixing near the surface. The increased influx is shared over a 1.625 times larger area, and thus surface averaged fluxes remain similar in magnitude. The turbulent flow has a net significant larger influx. This is mainly due to the 4.5 times higher flow rate and thus higher average concentration in the cell, but other factors will be discussed further in this section. In the turbulent flow, the threaded surface gives rise to a significantly higher flux downstream. This is likely explained by the surface texture further increasing the turbulence as the flow develops in the cell.

In Fig. 5 we present the experimentally observed deposited mass and compare it with extrapolated values based on the fluxes obtained from the CFD and PFM models. From the experiments, in both the laminar and turbulent flow, we observe that more mass is deposited on threaded surfaces. As the material is transported to the surface, the crystal growth is determined by either nucleation at new crystal sites or by growth on existing crystal surfaces. While the observation aligns with the higher expected influx in the turbulent case, the CFD results from the laminar studies indicate that the threaded surface experience a similar influx as the smooth surface (see Fig. 5c). However, the observed experimental deposition for the laminar case is significantly higher for the threaded compared to the smooth. This suggests that growth in the low influx regime is not only limited by the material influx.

A surface's potential for scaling could be characterized by its roughness [30]. As the nucleation sites on the clean surface, which in this study were characterized by  $Pa$ , are identical, it is not the amount of nucleation sites that govern the net deposition. Surface crystallization of low soluble salts has been proposed to be kink limited [49], i.e. more viable nucleation sites exist on the threaded surface. Therefore, the low influx regime's overall deposition is driven by favourable nucleation sites rather than by the overall influx. In the turbulent high influx regime, the material transport governs net deposition. The effect of increased injection rate on the deposited mass is identical for the two surface morphologies: with the same amount of liquid injected through the deposition cell, more mass is deposited under high influx. Fig. 3e shows that the mean flux is significantly increased for the threaded surface compared to the smooth surface under turbulent flow. Under

turbulent flow conditions, both smooth and threaded surfaces experience an increase in deposition, which is in line with the calculated influx. The observed mass deposition rate for the [Turbulent, threaded] setup is in line with that of the PFM model, exceeding the extrapolated rate obtained from the CFD simulations. This could either indicate that the effective kinetics are significantly faster than modelled or could be explained by attachment of upstream precipitate particles captured from the flow. The rest of the experiments show more mixed comparison with the extrapolated model fluxes.

Fig. 5c suggests that deposition is not the only process at play; detachment processes also affect the net deposition rate. In the low influx regime, there is evidence for a loss of mass between subsequent time steps. The impact of scale detachment on the net deposition rate can be investigated through the difference in mass between two experimental durations, ( $\Delta m = m(t_{i+1}) - m(t_i)$ ) see Fig. 5c). Hence,  $\Delta m < 0$  describes a case of detachment. There is an overall tendency for  $\Delta m$  to be larger on the smooth surface compared to the threaded in the low influx regime. This suggests that detachment processes are more prominent per detachment event on the smooth surface, while the threaded surface has a continuous removal of smaller amounts of deposited mass.

Under high material influx, the deposited mass consistently increased linearly as a function of injected fluid volume (see Fig. 5ab). In contrast, no clear increasing trend is observed under low influx. Since the mass deposited under high influx is observed to increase continuously with injected brine volume, it can be inferred that the impact of detachment is more pronounced in the low influx regime. Based on the results presented so far, no conclusion to the mechanism that causes more pronounced detachment under low influx can be established. It cannot be concluded whether the detachment behaviour occurs periodically or is part of an initial transient.

We have shown how deposition can be quantified through gravimetric data and that both scale attachment and detachment occur. However, to understand these processes, the surface crystal growth distribution must also be quantified.

### 3.2. Distribution of crystal deposits

To quantify the surface growth distribution, CT scans of deposition cells were performed before and after each study. An axial view of a magnified area of the 2D orthoslices is shown in Fig. 6 to emphasize the location and magnitude of scale deposition. 3D representation of one experiment with related CFD simulations is shown in Fig. 7. The

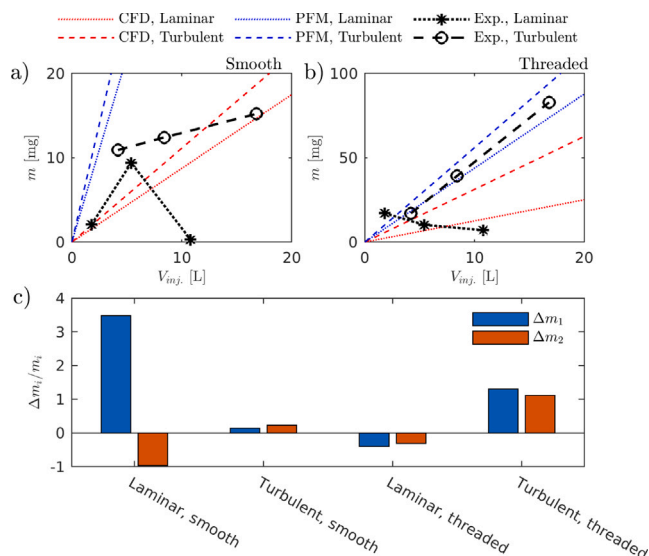


Fig. 5. Mass deposited as a function of injected brine  $v_{inj}$ , comparing experimental to PFM and CFD model on (a) smooth surfaces and (b) threaded surfaces as a function of injected brine. The CFD and PFM lines are based on the average deposition rates after they have reached a quasi-steady state. (c) Difference in mass ( $\Delta m$ ) deposited between the observations.  $\Delta m_i$  is defined as  $m(t_{i+1}) - m(t_i)$ , where  $t_i$  refers to the experimental time steps.

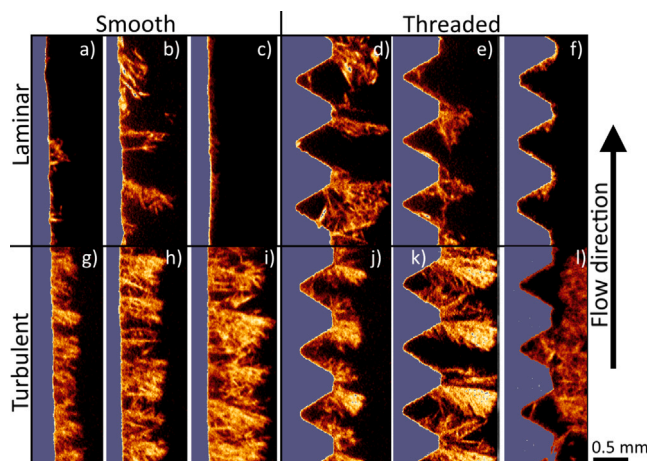


Fig. 6. Orthoslices of micro-CT scans showing a 3 mm long section of each sample. (a)-(c) and (g)-(i) refer to  $t_{L,1}$ ,  $t_{L,2}$ ,  $t_{L,3}$ , respectively. (d)-(f) and (j)-(l) refer to  $t_{T,1}$ ,  $t_{T,2}$ ,  $t_{T,3}$ , respectively.

full orthoslices are located in the Supplementary Material. In all cases (Fig. 6), the deposited crystals appear dendritic, similar to previous studies on BaSO<sub>4</sub> [50,51]. The deposition distribution vary with surface morphology and fluid hydrodynamics.

The deposition distribution across the threaded surface, observed in Fig. 6df and Fig. 6jl, supports that a spatial modulation of material influx exists. There exist a sizeable local influx of material on the threadings facing the fluid stream (Fig. 7a). By correlating the increased influx with the deposition distribution from Fig. 6jl and Fig. 7c it becomes evident that there is a strong correlation between the material influx and the location at which growth occurs.

The periodicity on the threaded surfaces imposes a material influx pattern which is nonexistent on the smooth surfaces. Therefore, on the smooth surfaces, there is no distinct pattern in which the scaling occurs in either the low or the high influx regimes.

There are two main effects of the effect of hydrodynamics that are present from Fig. 6. First, there is a difference in the deposition features between laminar and turbulent flow conditions. In the low influx regime, the scale is removed and rearranged as more brine is injected. At high material influx, the crystal growth on the threaded surface is located on the area with a locally high influx. Furthermore, the formed crystals possess a larger branching density from the primary dendrites compared to those from the laminar cases. As the experimental duration is increased, the following processes occur: The initiation of dendritic branching, followed by the merging of dendritic branches, and finally, the detachment of adhered crystals. The second effect is that the regime of influx determines the distribution of scale formation. In the low influx regime, crystal growth is localized in clusters and randomly distributed across the surface. Under high influx, the growth is uniformly distributed across the surface.

To quantify this distribution, the micro-CT tomographies were treated with the code previously described in Section 2.7. The output of the code is seen in Fig. 8 and shows a perspective view down the scanned segments, where the colorbar denotes the height deviation from an ellipsoid fitted to the mean plane. For example in Fig. 8.1a few clusters can be observed, while Fig. 8.3f shows a uniform deposition.

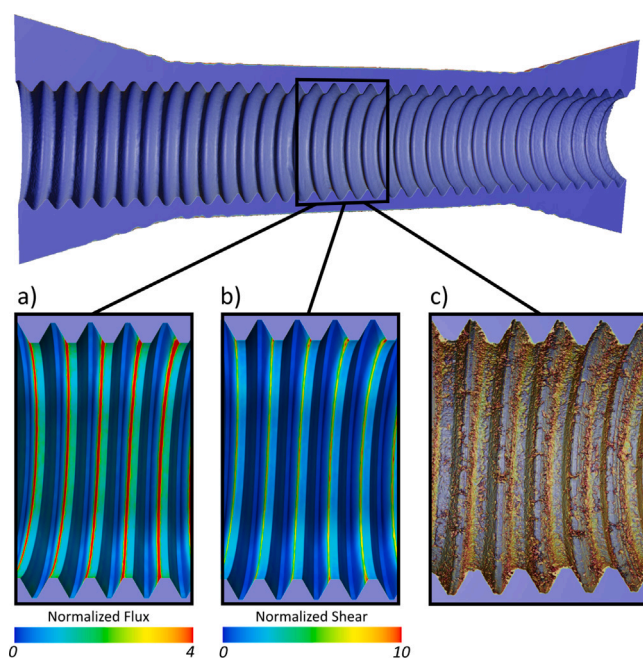


Fig. 7. Threaded surfaces at a high influx regime. (a) simulated time-averaged material influx, (b) simulated time-averaged shear forces and (c) location of scale deposition from CT tomography. The fluxes and shear forces are normalized with the surface-average of the deposition cell wall.

By tracking the average profile roughness ( $Pa$ ) and the spikiness of the crystal height distribution ( $Pku$ ) in successive order of the experimental duration, it becomes clear that two different physical mechanisms are at play.

For the first time step,  $t_{L,1}$ , on the smooth surface under low material influx (see Fig. 8.1a, growth occurred in a few scattered localized clusters. This is reflected in the low roughness and the large spikiness (see Fig. 9ab). At the next time step,  $t_{L,2}$ , deposition still occurs in clusters, but they are more evenly spread (Fig. 8.1b). This deposition characteristic is supported by the increased roughness and the decrease in spikiness. Finally, at  $t_{L,3}$ , (see Fig. 8.1c, only a few clusters can be observed. However, there is now a thin evenly spread layer of crystals all over the surface. At  $t_{L,3}$  for the smooth surface, the least amount of mass was deposited, however from Fig. 8.1c the deposition can be seen as an effect that has occurred on the whole surface, which in addition led to an increase in the roughness from  $t_{L,1}$ .

The same trend is observed for the threaded surface. While the smooth surface had the highest amount of mass at  $t_{L,2}$ , for the threaded cell under laminar conditions, the highest amount of deposited mass occurs at  $t_{L,1}$ . This is supported by the type of height distribution measured on the surface. The high roughness of the surface indicates a large mass deposition, while the low spikiness confirms that deposition is spread over multiple locations. At  $t_{L,2}$ , crystals were partially removed, and the deposited layer is more scattered. In comparison to the  $t_{L,2}$ , a decrease of the roughness has occurred, while there is a strong increase in the spikiness. Similarly to the data point for the smooth surface at  $t_{L,3}$ , a more uniformly distributed layer is observed. The changing type of height distribution indicates that the stage of growth can be tracked by the profile texture parameters. This trend of a change in deposition distribution as a function of time is not present in the high influx regime. Here, a new trend can be observed, that is shared across both the smooth and threaded surfaces. The crystals form an evenly distributed layer across the whole surface under these conditions. As mentioned, a more significant degree of dendritic branching and merging of deposited crystals are observed under turbulent conditions. Before branching, at  $t_{T,1}$ , a large roughness is observed, reflecting large local dendrites emerging from the surface. As the secondary branches merge, the roughness is decreased and the outermost layer becomes more smooth (Fig. 9b). The spikiness varies little (less than 1.5) at all experimental conditions, suggesting that the type of distribution does not change with time.

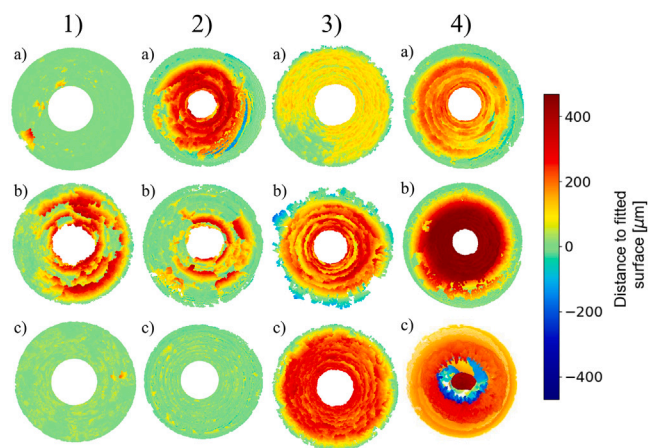


Fig. 8. Perspective view of the analysed cell section. The arrow indicates increased experimental duration. 1 = [Laminar, smooth], 2 = [Laminar, threaded], 3 = [Turbulent, smooth], 4 = [Turbulent, threaded]. (a), (b), and (c) refer to  $t_{L,1}$ ,  $t_{L,2}$ ,  $t_{L,3}$ , respectively. (d), (e), and (f) refer to  $t_{T,1}$ ,  $t_{T,2}$ ,  $t_{T,3}$ , respectively.

### 3.3. Flow dependent growth mechanism

Surface deposition rates are largely controlled by the material flux to the surface. From a thermodynamic consideration, growth is more energetically favourable on existing phases than the formation of a nucleus. A theory used to describe molecular self-assembly provides a framework for a deeper understanding of scaling growth in low and high influx regimes [52]. From molecular self-assembly, the rate governing regime growth can be classified as either thermodynamic or kinetic based on the competition between the diffusion of adsorbents and the magnitude of material influx [52]. In the thermodynamic regime, growth is limited by favourable nucleation sites, where on the contrary, the kinetic regime is when the material supply limits growth. In this study, the molecular surface diffusion is identical because the temperature and material of the surface are the same. However, there is a variation in the surface influx. For large material influx studies, the growth will be of a kinetic character i.e. the movement of a particle is confined to the spatial dimension of the surface and has a small mean path before it adheres completely, either on the pristine surface or with another particle. In the low influx regime, the growth governing mechanism will be of a thermodynamic character as the influx of material is low, resulting in only the most energetically favourable sites occupied [52].

At laminar flow conditions, deposition was observed at a limited number of sites. From this, we infer that nucleation has only occurred at the most thermodynamically favourable sites. Consequently, a phase space where thermodynamics play a more dominant role than the kinetics can be derived. Under turbulent flow, i.e. higher influx to the surface, the uniform deposition pattern suggests that growth and deposition have occurred in multiple nucleation sites. Under these conditions, it can therefore be stated that the contribution of kinetics is more significant than that of thermodynamics.

Local crystal growth is self-reinforcing in the low influx regime. As scale formation occurs in small clusters, this will modulate the flow by creating a shadow zone behind existing crystals. Thereby further transport of material to the surface is limited, and reaction with nucleation sites is inhibited. We illustrated the shadow zone by simulating the flow around a crystal (Fig. 10). Behind the crystal there is a reduced fluid saturation further downstream in the laminar flow condition than under the turbulent conditions. This difference is a consequence of the increased mixing from the eddies in the turbulent flow. This effect

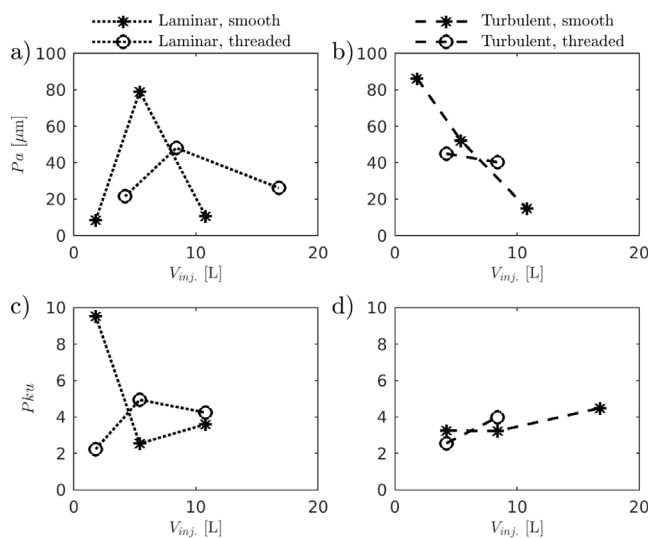


Fig. 9. Texture parameters observed after experiments. (a)  $P_a$  for laminar flow experiments. (b)  $P_a$  for turbulent flow experiments. (c)  $P_{ku}$  for laminar flow experiments. (d)  $P_{ku}$  for turbulent flow experiments.

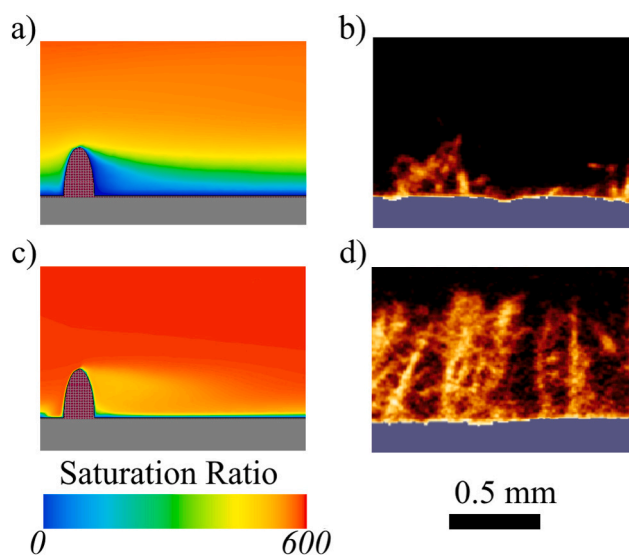


Fig. 10. Visualization of shadowing on a smooth surface. (a) CFD, laminar conditions (b) CT scan of crystal grown under laminar conditions. (c) CFD, turbulent conditions (d) CT scan of crystal grown under turbulent conditions.

is clearly observed from the experimental results in Fig. 10b and d, where the laminar flow conditions yield solitary crystals versus more and denser structures in the turbulent case.

Furthermore, the growth on the threading tops facing the fluid stream is enhanced by the increased fluid kinetic energy from turbulence. A temporal periodicity in the influx was revealed to exist on the threadings (see Fig. 11). A time series of the influx was extracted from the CFD model at the top, middle, and bottom of a threading. A correlated periodicity in the influx existed between the three positions. However, the signal from the top and middle positions appears more convoluted. The overall flux magnitude is lower at the bottom of the threading. As the kinetic energy and frequency is correlated, a higher kinetic energy state of the ions would be observed at the top positions on the threadings. The differences in the energy spectrum from the threading valleys to the tops provides further explanation to why there is a significantly higher amount of deposition on the top.

In Fig. 12, the mechanisms behind flow-dependent crystal growth are outlined. In the low influx regime, there are three key steps:

1. **Nucleation in clusters**, where the growth is spatially confined to local clusters, having a high spikiness. Here, deposition is limited by the density of favourable nucleation sites. A consequence of this is that higher deposition will be observed on threaded surfaces in the low influx regime as more viable nucleation sites exist. Solitary growth is self-reinforcing as low mixing in the shadow zones of existing crystals occurs.

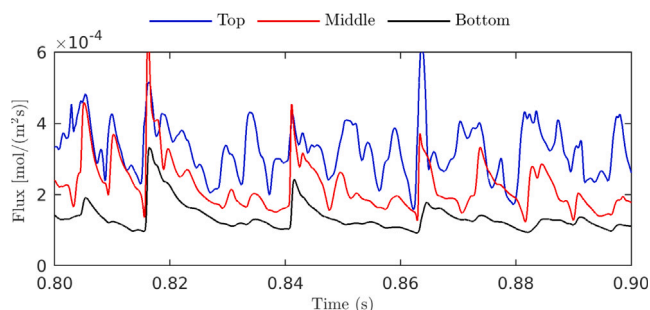


Fig. 11. Spatiotemporally resolved influx experienced by a threading; time series of three locations (top, middle and bottom) on the front of a threading.

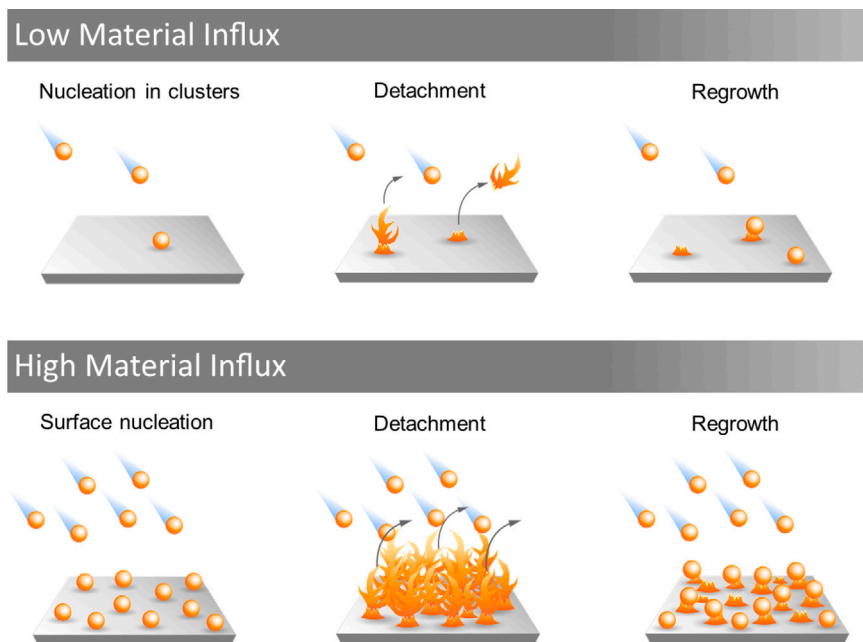


Fig. 12. Mechanistic principles behind the flow dependent growth. Orange spheres represent  $\text{BaSO}_4$ , either as incoming flux or deposited clusters. Low material influx favours local growth of dendrites, whereas many interlinked dendrites are favoured in the high material influx regime.

2. **Detachment** of the crystals occurs when they have reached a size where the forces exerted by the fluid becomes too large. Just before the detachment the growth is characterized by a very high surface roughness. However, as the mean line is shifted and the crystal height distribution is broader, a lower spikiness will be measured.
3. **Regrowth** of new clusters occur on pre-existing deposited material, reflected in an increased spikiness. Regrowth differs from the first step as secondary nucleation occurs on the roots of the detached particles. Thereby, a significantly lower energy is associated with regrowth, caused by the increase of nucleation sites due to the presence of pre-existing deposited material.

Similarly, crystal formation at high material influx conditions can be divided into three key steps:

1. **Initial surface nucleation** is the result of a large influx of material to the surface, and growth occurs as a global phenomenon occupying a larger density of nucleation sites and not only the most favourable sites. Here, the growth rate is kinetically limited as the growth is uniform across the surface. This is confirmed by the low spikiness observed.
2. **Detachment** in the regime with high material influx to the surface occurs with crystals exhibiting a larger height. This is due to the dendritic branching that interlocks existing crystals, giving them an increased surface attachment strength.
3. **Regrowth** will occur after the detachment, however, under turbulent flow conditions, this will be identical to initial surface nucleation, as the deposition is not spatially confined but is seen across the whole surface.

The growth mechanisms described above confirm the observations for laminar flow. Even though the total amount of mass on the surface does not increase with injected fluid, the crystals will be redistributed continuously. This creates a gradually increasing dense crystal layer, resulting in an eventual complete blocking of the cell, impeding the fluid flow. As crystals formed under laminar flow grow locally they will have a relatively small area adhered to the surface. As the shear forces and momentum on the crystals increase with their increasing length, the maximum tension they can withstand will depend on their

surface attachment area. As they are not interlinked to other crystals, which is the case in the high influx regime, they will have a relatively weak attachment. On the other hand, crystals formed in the high influx regime will be interconnected and therefore have a relatively larger area of contact to the surface than the crystals formed under low influx.

#### 3.4. Implications for future prediction models and field operators

The findings of this work demonstrate the importance of accounting for detachment in a comprehensive prediction of scale build-up. Previous prediction models have overestimated fouling rates because either the effect of detachment was not accounted for [53] or not incorporated correctly [54]. Newer models, accounting for the effect of scale detachment and attachment strength, have also been developed [26,55]. However, these models are insufficient, as their description of scale attachment strength is incomprehensive. We have shown in Section 3.2 that the distribution of crystal on the surface is directly linked to the surface attachment strength. These models fail because they do not account for crystal distribution. Consequently, detachment processes cannot be addressed comprehensively. To create a unified prediction model, it would be necessary to describe surface attachment strength accurately.

Real-world challenges exist where field operators experience the consequences of crystal distribution. For example, in transport pipelines, scaling and corrosion will, throughout its life-cycle, change the surface texture and alter the fouling formation rate. We have shown how deposition will vary in a non-linear manner throughout the life-time of production equipment. A smooth newly fabricated pipeline will experience a random distribution, whereas a worn surface will agitate turbulence in the fluid flow and reduce energy requirements for surface deposition, thereby reinforcing scale deposition.

Ageing of fouling deposit is the temporal transformation of a deposited layer and is considered one of the principal mechanistic stages of overall deposition [25]. In heat exchangers, ageing is seen to drastically increase fouling rate at production equipment's end life-time [34]. Our findings demonstrate how detachment can occur after a longer period when there is a larger interlocking between deposited scale. Scale removal devices based on fluid agitation operates on these basic mechanisms [56]. Based on our findings, the mechanism of this device can

be deduced. As crystal growth is removed before interlocking occurs, the crystal distribution is of a singular manner. This prevents larger sections from interlocking, and overall scale deposition is minimized as the surface attachment strength is lowered.

The nature of fouling is complex and determines the strength of the surface attachment. Crystallization fouling, adhering through nucleation, has a strong attachment, while biological fouling has a weaker adherence to the surface [57]. Biofouling was reduced in decentralized wastewater treatment operating at low aeration shear force [58]. Our findings support the notion that the deposition distribution and its interaction with shear forces will redistribute the fouling layer, resulting in a more dense layer being formed over time. This layer is known to be more resistant to mechanical removal [57]. Therefore, to understand the net formation of fouling, the distribution of deposition must be considered.

The distribution of fouling deposition has real-world implications, where the spatial modulation of fluid will create a deposition distribution, which will reinforce itself over time. The interlocking of crystals results in stronger attachment strength, and by minimizing the interconnection between deposited material, overall deposition can be reduced. As singular crystals are iteratively redistributed, more resilient scaling is formed.

#### 4. Conclusion

In summary, we revealed novel insights about scaling. We show that the impact of attachment and detachment processes is surface and flow-dependent. Smooth surfaces experience an areal uniform material influx, as demonstrated by the random deposition observed, irrespective of the flow regime. Threaded surfaces modulate flow profile and increased material influx locally; this variation in material influx caused patterned deposition distribution. Flow facing protuberances have a high deposition, which can be correlated to the areas where the material is transported. Areas with low material transport (such as valleys and the shadow side of the threads) showed reduced surface deposition. In the laminar low influx regime, solitary crystals formed due to few nucleation sites being occupied. The increase in favourable nucleation site on threaded surfaces acted as a growth template, thereby increasing formation on threaded surfaces compared to the smooth. The formation of these crystals created a shadow region behind them, decreasing the likelihood for further growth. Calculations of shear stress distribution revealed a correlation between locations of high shear forces and detachment processes of solitary crystals. Deposits on threaded surfaces experienced more local shear stress, which likely resulted in more frequent detachment of material on the threaded surfaces than on the smooth. Consequently, iterative detachment processes resulted in an increasingly dense adhered layer. In the turbulent high material influx regime, numerous nucleation sites were occupied; this is in contrast to the confined crystals observed under low material influx. Interlocking crystal branches increase surface attachment strength, thereby delaying detachment events.

Combining these mechanistic insights provides a template for scaling prediction models to be developed where the importance of material detachment, surface texture, and influx regimes are incorporated.

#### Acknowledgments

The authors acknowledge the Danish Underground Consortium (TotalEnergies, E&P Denmark, Noreco & Nordsofonden). This work was funded by the Danish Hydrocarbon Research and Technology Centre (DHRTC) under the CTR2 program. The authors also acknowledged the 3D Imaging Center (3DIM) at The Technical University of Denmark (DTU) for their support on X-ray computed tomography acquisition.

#### Declaration of competing interest

The authors declare that they have no known competing financial interests or personal relationships that could have appeared to influence the work reported in this paper.

#### Appendix A. Supplementary data

Supplementary material related to this article can be found online at <https://doi.org/10.1016/j.cej.2021.132583>.

#### References

- [1] K.M. Sassi, I.M. Mujtaba, Optimal design and operation of reverse osmosis desalination process with membrane fouling, *Chem. Eng. J.* 171 (2) (2011) 582–593, <http://dx.doi.org/10.1016/j.cej.2011.04.034>.
- [2] I. Sreedhar, S. Khaitan, R. Gupta, B.M. Reddy, A. Venugopal, An odyssey of process and engineering trends in forward osmosis, *Environ. Sci. Water Res. Technol.* 4 (2) (2018) 129–168, <http://dx.doi.org/10.1039/c7ew00507e>.
- [3] A. Deshmukh, C. Boo, V. Karanikola, S. Lin, A.P. Straub, T. Tong, D.M. Warsinger, M. Elimelech, Membrane distillation at the water-energy nexus: Limits, opportunities, and challenges, *Energy Environ. Sci.* 11 (5) (2018) 1177–1196, <http://dx.doi.org/10.1039/c8ee00291f>.
- [4] R. Sharifian, R.M. Wagterveld, I.A. Digdaya, C. Xiang, D.A. Vermaas, Electrochemical carbon dioxide capture to close the carbon cycle, *Energy Environ. Sci.* 14 (2) (2021) 781–814, <http://dx.doi.org/10.1039/D0EE03382K>.
- [5] J. Li, M. Tang, Z. Ye, L. Chen, Y. Zhou, Scale formation and control in oil and gas fields: A review, *J. Dispersion Sci. Technol.* 38 (5) (2017) 661–670, <http://dx.doi.org/10.1080/01932691.2016.1185953>.
- [6] Q. Zhao, Y. Liu, C. Wang, S. Wang, H. Müller-Steinhagen, Effect of surface free energy on the adhesion of biofouling and crystalline fouling, *Chem. Eng. Sci.* 60 (17) (2005) 4858–4865, <http://dx.doi.org/10.1016/j.ces.2005.04.006>.
- [7] G. Geovani, M. Argueta, Rehabilitation of geothermal wells with scaling problems, Technical Report, The United Nations University, 1995, pp. 207–240.
- [8] H. Müller-Steinhagen, Heat transfer fouling: 50 years after the Kern and Seaton model, *Heat Transfer Eng.* 32 (1) (2011) 1–13, <http://dx.doi.org/10.1080/01457632.2010.505127>.
- [9] R. Boch, A. Leis, E. Haslinger, J.E. Goldbrunner, F. Mittermayr, H. Fröschl, D. Hippler, M. Dietzel, Scale-fraction formation impairing geothermal energy production: interacting H<sub>2</sub>S corrosion and CaCO<sub>3</sub> crystal growth, *Geotherm. Energy* 5 (1) (2017) 4, <http://dx.doi.org/10.1186/s40517-017-0062-3>.
- [10] A. Boersma, F. Vercauteren, H. Fischer, F. Pizzocolo, Scaling assessment, inhibition and monitoring of geothermal wells, in: *43rd Workshop on Geothermal Reservoir Engineering*, 2018, pp. 1–13.
- [11] A. Ruiz-García, N. Melián-Martel, I. Nuez, Short review on predicting fouling in RO desalination, *Membranes* 7 (4) (2017) 1–17, <http://dx.doi.org/10.3390/membranes7040062>.
- [12] A. Alabi, M. Chiesa, C. Garlisi, G. Palmisano, Advances in anti-scale magnetic water treatment, *Environ. Sci. Water Res. Technol.* 1 (4) (2015) 408–425, <http://dx.doi.org/10.1039/c5ew00052a>.
- [13] A. Yi-Tsung Lu, A.T. Kan, M.B. Tomson, Nucleation and crystallization kinetics of barium sulfate in the hydrodynamic boundary layer: An explanation of mineral deposition, *Cryst. Growth Des.* 21 (3) (2021) 1443–1450, <http://dx.doi.org/10.1021/acs.cgd.0c01027>.
- [14] M.A. Jafar Mazumder, A review of green scale inhibitors: Process, types, mechanism and properties, *Coatings* 10 (10) (2020) 1–29, <http://dx.doi.org/10.3390/coatings10100928>.
- [15] D. Hasson, H. Shemer, A. Sher, State of the art of friendly “green” scale control inhibitors: A review article, *Ind. Eng. Chem. Res.* 50 (12) (2011) 7601–7607, <http://dx.doi.org/10.1021/ie200370v>.
- [16] R. Benvie, T. Chen, S. Heath, P. Chen, H. Montgomerie, T. Hagen, New environmentally acceptable chemistry and evaluation methods for scale inhibitor testing under turbulent flow and harsh scaling conditions, in: *SPE International Oilfield Scale Conference and Exhibition*, 2012, pp. 1–12, <http://dx.doi.org/10.2118/155428-MS>.
- [17] Z.J. Dai, Y.T. Lu, A. Kan, C. Leschied, Y. Zhao, C. Dai, X. Wang, S. Paudyal, S. Ko, M. Tomson, A mechanistic software platform for mineral surface deposition and inhibition prediction under different flow conditions, *Desalination* 509 (January) (2021) 115071, <http://dx.doi.org/10.1016/j.desal.2021.115071>.
- [18] T. Karmakar, P.M. Piaggi, M. Parrinello, Molecular dynamics simulations of crystal nucleation from solution at constant chemical potential, *J. Chem. Theory Comput.* 15 (12) (2019) 6923–6930, <http://dx.doi.org/10.1021/acs.jctc.9b00795>.
- [19] B.U. Anabaraonye, J.R. Bentzon, I. Khaliqdad, K.L. Feilberg, S.I. Andersen, J.H. Walther, The influence of turbulent transport in reactive processes: A combined numerical and experimental investigation in a Taylor-Couette reactor, *Chem. Eng. J.* (2021) 129591, <http://dx.doi.org/10.1016/j.cej.2021.129591>.

- [20] A. Quddus, I. Allam, BaSO<sub>4</sub> scale deposition on stainless steel, *Desalination* 127 (3) (2000) 219–224, [http://dx.doi.org/10.1016/S0011-9164\(00\)00012-6](http://dx.doi.org/10.1016/S0011-9164(00)00012-6).
- [21] Q. Wang, T. Chen, F. Al-Dawood, New understanding on calcium carbonate scaling kinetics, in: NACE - International Corrosion Conference Series, 2019.
- [22] A.B. BinMerdhah, A.A.M. Yassin, M.A. Muherei, Laboratory and prediction of barium sulfate scaling at high-barium formation water, *J. Pet. Sci. Eng.* 70 (1) (2010) 79–88, <http://dx.doi.org/10.1016/j.petrol.2009.10.001>.
- [23] M. Tranter, M. De Lucia, M. Wolfgramm, M. Kühn, Barite scale formation and injectivity loss models for geothermal systems, *Water* 12 (11) (2020) <http://dx.doi.org/10.3390/w12113078>.
- [24] E.F. Somerscales, Fundamentals of corrosion fouling, *Exp. Therm. Fluid Sci.* 14 (4) (1997) 335–355, [http://dx.doi.org/10.1016/S0894-1777\(96\)00136-7](http://dx.doi.org/10.1016/S0894-1777(96)00136-7).
- [25] N. Epstein, Thinking about heat transfer fouling: A 5 × 5 matrix, *Heat Transfer Eng.* 4 (1) (1983) 43–56, <http://dx.doi.org/10.1080/01457638108939594>.
- [26] Z. Han, Z. Xu, X. Yu, CFD modeling for prediction of particulate fouling of heat transfer surface in turbulent flow, *Int. J. Heat Mass Transfer* 144 (2019) 118428, <http://dx.doi.org/10.1016/j.ijheatmasstransfer.2019.07.078>.
- [27] D. Yang, J. Liu, E. Xiaoxue, L. Jiang, Model for seawater fouling and effects of temperature, flow velocity and surface free energy on seawater fouling, *Chin. J. Chem. Eng.* 24 (5) (2016) 658–664, <http://dx.doi.org/10.1016/j.cjche.2016.01.012>.
- [28] A.J. Karabelas, Scale formation in tubular heat exchangers - Research priorities, *Int. J. Therm. Sci.* 41 (7) (2002) 682–692, [http://dx.doi.org/10.1016/S1290-0729\(02\)01363-7](http://dx.doi.org/10.1016/S1290-0729(02)01363-7).
- [29] M.J. Li, S.Z. Tang, F. long Wang, Q.X. Zhao, W.Q. Tao, Gas-side fouling, erosion and corrosion of heat exchangers for middle/low temperature waste heat utilization: A review on simulation and experiment, *Appl. Therm. Eng.* 126 (2017) 737–761, <http://dx.doi.org/10.1016/j.applthermaleng.2017.07.095>.
- [30] M.M. Vazirian, T.V. Charpentier, M. de Oliveira Penna, A. Neville, Surface inorganic scale formation in oil and gas industry: As adhesion and deposition processes, *J. Pet. Sci. Eng.* 137 (2016) 22–32, <http://dx.doi.org/10.1016/j.petrol.2015.11.005>.
- [31] X. Xing, C. Ma, Y. Chen, Mechanism of calcium carbonate scale deposition under subcooled flow boiling conditions, *Chin. J. Chem. Eng.* 13 (4) (2005) 464–470, <http://citeseerx.ist.psu.edu/viewdoc/summary?doi=10.1.1.463.3717>.
- [32] G. Graham, L. Boak, C. Hobden, Examination of the effect of generically different scale inhibitor species (PPCA and DETPMP) on the adherence and growth of barium sulphate scale on metal surfaces, in: SPE International Oilfield Scale Conference and Exhibition, 2001, pp. 1–15, <http://dx.doi.org/10.2118/68298-MS>.
- [33] M. Pourbozorg, T. Li, A.W. Law, Effect of turbulence on fouling control of submerged hollow fibre membrane filtration, *Water Res.* 99 (2016) 101–111, <http://dx.doi.org/10.1016/j.watres.2016.04.045>.
- [34] A. Janzen, E.Y. Kenig, S.E. Gmbh, R. Federation, Understanding and analysis of fouling behavior of bare-wire heating elements in electric water heating, in: *Heat Exchanger Fouling and Cleaning*, 2019, pp. 1–8.
- [35] S. Keysar, R. Semiat, D. Hasson, J. Yahalom, Effect of surface roughness on the morphology of calcite crystallizing on mild steel, *J. Colloid Interface Sci.* 162 (2) (1994) 311–319, <http://dx.doi.org/10.1006/jcis.1994.1044>.
- [36] S. Kazi, G. Duffy, X. Chen, Mineral scale formation and mitigation on metals and a polymeric heat exchanger surface, *Appl. Therm. Eng.* 30 (14–15) (2010) 2236–2242, <http://dx.doi.org/10.1016/j.applthermaleng.2010.06.005>.
- [37] V. Eroini, N. Kapur, A. Neville, M. Euvrard, Preventing scale formation using modified surfaces, in: NACE - International Corrosion Conference Series, 2011, pp. 1–15.
- [38] H. Wang, V. Alfredsson, J. Tropsch, R. Ettl, T. Nylander, Formation of CaCO<sub>3</sub> deposits on hard surfaces - Effect of bulk solution conditions and surface properties, *ACS Appl. Mater. Interfaces* 5 (10) (2013) 4035–4045, <http://dx.doi.org/10.1021/am401348v>.
- [39] A.K. Halvey, B. Macdonald, A. Dhyani, A. Tuteja, Design of surfaces for controlling hard and soft fouling, *Philos. Trans. R. Soc. A* 377 (2138) (2019) 20180266, <http://dx.doi.org/10.1098/rsta.2018.0266>.
- [40] N. Gathimba, Y. Kitane, T. Yoshida, Y. Itoh, Surface roughness characteristics of corroded steel pipe piles exposed to marine environment, *Constr. Build. Mater.* 203 (2019) 267–281, <http://dx.doi.org/10.1016/j.conbuildmat.2019.01.092>.
- [41] C. Klingaa, T. Dahmen, S. Baier, S. Mohanty, J. Hattel, X-ray CT and image analysis methodology for local roughness characterization in cooling channels made by metal additive manufacturing, *Addit. Manuf.* 32 (2020) 101032, <http://dx.doi.org/10.1016/j.addma.2019.101032>.
- [42] K.S. Pitzer, Thermodynamics of electrolytes. I. Theoretical basis and general equations, *J. Phys. Chem.* 77 (2) (1973) 268–277, <http://dx.doi.org/10.1021/j100621a026>.
- [43] B.Y. Zhen-Wu, K. Dideriksen, J. Olsson, P.J. Raahauge, S.L. Stipp, E.H. Oelkers, Experimental determination of barite dissolution and precipitation rates as a function of temperature and aqueous fluid composition, *Geochim. Cosmochim. Acta* 194 (2016) 193–210, <http://dx.doi.org/10.1016/j.gca.2016.08.041>.
- [44] Z. Dai, F. Zhang, F. Yan, N. Bhandari, G. Ruan, Z. Zhang, Y. Liu, H.A. Alsaiani, Y.T. Lu, G. Deng, A.T. Kan, M. Tomson, A new theoretical model for the induction time and scale inhibitor dosage predictions for calcite and barite over wide ranges of temperature, inhibition concentration and saturation index, in: SPE International Symposium on Oilfield Chemistry, 2017, pp. 647–657, <http://dx.doi.org/10.2118/184547-ms>.
- [45] D. Bosbach, Linking molecular-scale barite precipitation mechanisms with macroscopic crystal growth rates, in: *Water-Rock Interactions, Ore Deposits, and Environmental Geochemistry: A Tribute to David A. Crerar, 2002*, pp. 97–110.
- [46] F. Yang, A.G. Stack, V. Starchenko, Micro-continuum approach for mineral precipitation, *Sci. Rep.* 11 (1) (2021) 1–14, <http://dx.doi.org/10.1038/s41598-021-82807-y>.
- [47] F.M. White, *Fluid Mechanics*, seventh ed., McGraw Hill, Inc., 2011.
- [48] A. Ivask, I. Kurvet, K. Kasemets, I. Blinova, V. Aruoja, S. Suppi, H. Vija, A. Käkinen, T. Titma, M. Heinlaan, M. Visnapuu, D. Koller, V. Kisand, A. Kahru, Size-dependent toxicity of silver nanoparticles to bacteria, yeast, algae, crustaceans and mammalian cells in vitro, *PLoS One* 9 (7) (2014) 102108, <http://dx.doi.org/10.1371/journal.pone.0102108>.
- [49] J.J. De Yoreo, L.A. Zepeda-Ruiz, R.W. Friddle, S.R. Qiu, L.E. Wasylenki, A.A. Chernov, G.H. Gilmer, P.M. Dove, Rethinking classical crystal growth models through molecular scale insights: Consequences of kink-limited kinetics, *Cryst. Growth Des.* 9 (12) (2009) 5135–5144, <http://dx.doi.org/10.1021/cg900543g>.
- [50] J.M. García-Ruiz, F. Otálora, Crystal growth in geology: Patterns on the rocks, in: *Handbook of Crystal Growth: Bulk Crystal Growth: Second Edition*, second ed., 2015, pp. 1–43, <http://dx.doi.org/10.1016/B978-0-444-63303-3.00001-8>.
- [51] N.S. Dera, F. Fatra, G. Ivanto, S. Muryanto, A.P. Bayuseno, Phase analysis and crystal morphology of barium sulphate precipitated from the laminar flowing water, in: IOP Conference Series: Materials Science and Engineering, vol. 202, 2017, 012029, <http://dx.doi.org/10.1088/1757-899X/202/1/012029>.
- [52] J.V. Barth, G. Costantini, K. Kern, Engineering atomic and molecular nanostructures at surfaces, *Nature* 437 (7059) (2005) 671–679, <http://dx.doi.org/10.1038/nature04166>.
- [53] D. Hasson, M. Avriel, W. Resnick, T. Rozenman, S. Windreich, Mechanism of calcium carbonate scale deposition on heat-transfer surfaces, *Ind. Eng. Chem. Fundam.* 7 (1) (1968) 59–65, <http://dx.doi.org/10.1021/i160025a011>.
- [54] X. Yang, W. Li, L. Guo, X. Liu, H. Feng, Prediction of CaCO<sub>3</sub> scaling in water injection wellbore, *Appl. Therm. Eng.* 98 (2016) 532–540, <http://dx.doi.org/10.1016/j.applthermaleng.2015.12.048>.
- [55] C. Paz, E. Suárez, M. Conde, J. Vence, Development of a computational fluid dynamics model for predicting fouling process using dynamic mesh model, *Heat Transfer Eng.* 41 (2) (2020) 199–207, <http://dx.doi.org/10.1080/01457632.2018.1522108>.
- [56] A. Krueger, F. Pouponnot, P. Houston, S.A. Petroval, Heat exchanger performance enhancement through the use of tube inserts in refineries and chemical plants – successful applications, in: *International Conference on Heat Exchanger Fouling and Cleaning VIII*, 2009, pp. 399–406.
- [57] S. Fernandes, I.B. Gomes, L.C. Simões, M. Simões, Overview on the hydrodynamic conditions found in industrial systems and its impact in (bio)fouling formation, *Chem. Eng. J.* 418 (2021) 129348, <http://dx.doi.org/10.1016/j.cej.2021.129348>.
- [58] A. Ding, H. Liang, G. Li, N. Derlon, I. Szivak, E. Morgenroth, W. Pronk, Impact of aeration shear stress on permeate flux and fouling layer properties in a low pressure membrane bioreactor for the treatment of grey water, *J. Membr. Sci.* 510 (2016) 382–390, <http://dx.doi.org/10.1016/j.memsci.2016.03.025>.